

Denoising human cardiac diffusion tensor magnetic resonance images using sparse representation combined with segmentation

L J Bao¹, Y M Zhu^{1,2}, W Y Liu^{1,2}, P Croisille², Z B Pu¹, M Robini²
and I E Magnin¹

¹ HIT—INSA Sino French Research Centre for Biomedical Imaging, Harbin Institute of Technology, Harbin, People's Republic of China

² CREATIS-LRMN, CNRS UMR 5220, Inserm U630, INSA of Lyon, University of Lyon 1, Villeurbanne, France

E-mail: baolij@gmail.com

Received 20 May 2008, in final form 18 January 2009

Published 13 February 2009

Online at stacks.iop.org/PMB/54/1435

Abstract

Cardiac diffusion tensor magnetic resonance imaging (DT-MRI) is noise sensitive, and the noise can induce numerous systematic errors in subsequent parameter calculations. This paper proposes a sparse representation-based method for denoising cardiac DT-MRI images. The method first generates a dictionary of multiple bases according to the features of the observed image. A segmentation algorithm based on nonstationary degree detector is then introduced to make the selection of atoms in the dictionary adapted to the image's features. The denoising is achieved by gradually approximating the underlying image using the atoms selected from the generated dictionary. The results on both simulated image and real cardiac DT-MRI images from *ex vivo* human hearts show that the proposed denoising method performs better than conventional denoising techniques by preserving image contrast and fine structures.

(Some figures in this article are in colour only in the electronic version)

1. Introduction

Diffusion tensor magnetic resonance imaging (DT-MRI) is at present the only means for *in vivo* and nondestructive characterization of the three-dimensional (3D) diffusion and fibre architecture of human anatomical organs such as brain white matter (Basser *et al* 1994), skeletal muscle (Galban *et al* 2005), spinal cord (Schwartz *et al* 2005) and myocardium (Scollan and Holmes 2000). It is well known that myocardial fibre orientation is altered in various cardiac diseases such as myocardial infarction, ischaemic heart disease and ventricular

hypertrophy (Wu and Tseng 2006). Therefore, detailed information about 3D fibre structures of myocardium can provide important cues to the understanding of the heart's physiological and functional properties, and to the diagnosis of heart diseases. However, cardiac DT-MRI is highly susceptible to noise. The noise, primarily at the level of diffusion-weighted image (DWI), obeys a Rician distribution (Gudbjartsson and Patz 1995, Macovski 1996). The noise in DT-MRI is the subject of several papers (Basser and Pajevic 2000, Koay *et al* 2007). The noise in DWIs produces errors in the subsequent calculations of the tensor, eigenvalues, eigenvectors, mean diffusivity (MD), diffusion anisotropy indices (DAIs) and fibre orientations. These errors include, for example, positive bias in fractional anisotropy (FA), negative eigenvalues, disorder of the eigenvectors and tracked fibres. So improving the signal-to-noise ratio (SNR) is crucial for practical utility of DT-MRI in human hearts, and noise removal techniques constitute the most efficient way without additional acquisitions.

Numerous denoising algorithms have been proposed for magnetic resonance (MR) images in the past decades (Awate and Whitaker 2007, Basu *et al* 2006, Gerig and Kubler 1992, Gilboa *et al* 2004, Hamarneh and Hradsky 2007). At present, the widely used denoising methods are based on the partial-differential-equation (PDE) filter (Perona and Malik 1990) and wavelet algorithm. The PDE filter, also known as the anisotropic or nonlinear diffusion filter, uses different smoothing degrees proportional to local intensity gradient and can preserve image edges. It has been employed to filter both scalar images (Chen and Edward 2005) and DT-MRI eigenvector fields (Arsigny *et al* 2006). However, PDE methods can yield good results only for low noise levels. For high noise levels, their denoising performance is unsatisfactory due to the serious degradation in contrast. Wavelet-based denoising has also been applied to MR images to achieve a general improvement in image quality (Nowak 1999, Wirestam and Bibic 2006). Denoising based on the wavelet transform, like the Fourier transform and the discrete cosine transform, operates on all information in the data: the image to be denoised is firstly transformed by means of predefined basis functions, and then an inverse transform is performed after thresholding the transform coefficients. In this condition, not only the useful information but also the noise in the image is involved in the convolution with the basis functions during the transformation. Moreover, how to determine the threshold is also a problem that limits the accuracy of the final result.

Recently, sparse representation has appeared as a promising theory for many signal and image processing problems such as compression, independent component analysis, image inpainting, regularization and denoising, proposed in Elad and Aharon (2006), Pham and Smeulders (2006) and Starck *et al* (2005), respectively. Unlike classical approaches, sparse representation-based denoising (SPDN) is achieved by selecting underlying information in the data with the aid of atoms generated from different function bases or database. The selection of function bases should correspond to the data features. Generally, images in practice are usually highly structured since their pixels exhibit strong dependences, especially when they are spatially proximate, and these dependences carry important information about the structure of the objects. On the other hand, the noise in the image distributes randomly without any organized structure. So even if an image is deteriorated by noise, its structure features can still be approximated with suitable atoms.

The performance of SPDN strongly depends on the denoising model and the dictionary. Indeed, the denoising model is a linear programming problem with two constraints: approximation stop criterion and sparsity of the representation coefficients. Based on an estimation of the noise intensity, the approximation stop criterion is set up to control the approximation procedure. As for the sparsity constraint, it relies on the property of the dictionary, so it is critical to generate appropriate dictionary according to the structures in the observed image. Considering that a real image often contains various contents, a

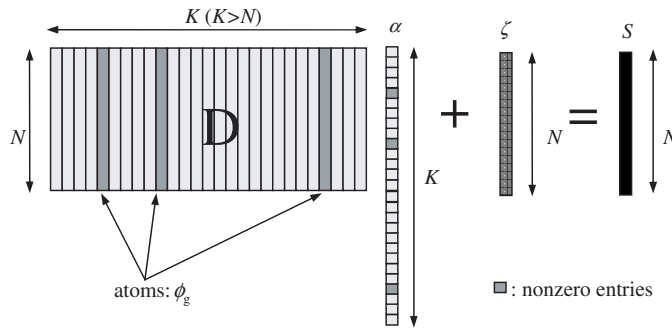


Figure 1. Principle of sparse representation.

dictionary with multiple bases was proposed in Granai and Vandergheynst (2004), which is a salient property of SPDN. Starck *et al* (2005) applied multiple bases to separate the overlapped textures from underlying image content by employing each basis to represent the whole image respectively. The method requires that every basis in the dictionary should be very selective, or it is prone to causing approximation errors. Also note that it is often inefficient to use one basis to represent the whole image.

In this paper, we develop the current sparse representation to denoise human cardiac DT-MRI data and to examine its effectiveness in improving the quality of DWI, as well as the accuracy of fibre orientation computation. We propose a segmentation-guided SPDN method based on the use of a segmentation mechanism for guiding the choice of suitable bases in the dictionary, thus making the decomposition process more adaptive and efficient. The segmentation employs the concept of nonstationarity degree (NSD), which is particularly robust for dealing with noisy data. The proposed method is evaluated on the simulated heart image and ten *ex vivo* human hearts, and compared to the PDE-based method (Catte *et al* 1992) and the wavelet-based method (Pizurica *et al* 2003).

2. Theory

2.1. Sparse representation

Sparse representation, also referred to as ‘atom decomposition’ or ‘sparse approximation’, evolved from non-redundancy orthogonal transformation. It is aimed at representing a given signal $S \in \mathfrak{R}^N$ by a linear combination of a few atoms $\phi_g \in \mathfrak{R}^N$ extracted from a dictionary $D \in \mathfrak{R}^{N \times K}$ of K atoms. The sparsity comes from the fact that only a small number of atoms are used. This corresponds to solving the following optimization problem:

$$\alpha^{\text{opt}} = \arg \min_{\alpha \in \mathfrak{R}^K} \|\alpha\|_0 \quad \text{subject to} \quad S = D\alpha + \xi, \quad 0 \leq \xi < S, \quad (1)$$

where, as illustrated in figure 1, $\|\alpha\|_0$ stands for the number of nonzero entries in representation coefficient vector $\alpha \in \mathfrak{R}^K$, ξ is the approximation error that, in the ideal case, approximates to zero and $D \in \mathfrak{R}^{N \times K}$ is a dictionary of K atoms ϕ_g which satisfies $D = \{\phi_g \in \mathfrak{R}^N \mid \|\phi_g\| = 1, g \in K\}$.

Usually, dictionaries are overcomplete with $K > N$. Atoms (represented by columns in figure 1) are the primary elements of a dictionary and their size is the same as that of the signal in solution. In sparse representation, atoms are generated from parameterized basis functions such as wavelets, curvelet, ridgelet, contourlet, etc. or adaptive trained database (Aharon *et al* 2006). The atoms generated from the same basis function constitute a basis. A dictionary can

include either a single basis or multiple bases that make it possible to better represent complex signals with different feature structures. The given signal S is approximately represented by $\hat{S} = D\alpha^{\text{opt}}$.

Therefore, selecting the optimal linear combination of atoms from a dictionary to approximate the underlying data is an NP-hard problem (nondeterministic polynomial time hard problem), for which a few algorithms have been proposed: matching pursuit (MP, Mallat and Zhang 1993), basis pursuit (BP, Chen *et al* 1998) and focal under determined system solver (FOCUSS, Gorodnitsky and Rao 1997). The MP is a greedy pursuit algorithm that selects the best suitable atoms sequentially in iteration, while the BP is a global optimal algorithm that finds the sparse representation atoms by convex optimization based on minimizing the l^1 norm of the representation coefficients. The FOCUSS is similar to the BP by minimizing the l^p norm of the representation coefficients. However, the BP and FOCUSS algorithms have high computational cost and in some case, compromised convergence. So, for computational simplicity and robustness, we adopt the MP algorithm in this work.

2.2. Image denoising based on sparse representation

Theoretically, sparse representation of an image is the same as that of a signal except that it is a dictionary composed of 2D atoms. Generally speaking, image denoising based on sparse representation attempts to extract underlying structures from the observed image by representing it with a proper dictionary, whereas the noise is left and is not represented because it exhibits no structure feature. The process of approximation is controlled by a stop criterion, determination of which relies on the noise level of the image, the tolerated approximation error and the constraint on sparsity.

Let $y \in \mathfrak{R}^{N \times N}$ be the observed noisy image of the form

$$y = x + r, \quad (2)$$

where x denotes the noise-free image, and r is an additive noise with standard deviation σ_r .

According to the sparse representation, the observed noisy image y can be represented by a column vector $y \in \mathfrak{R}^{N^2}$ as

$$y = D\alpha^{\text{opt}} + \xi + r, \quad (3)$$

where dictionary $D \in \mathfrak{R}^{N^2 \times K}$ and $\alpha^{\text{opt}} \in \mathfrak{R}^K$ with $K > N^2$.

Actually, each atom in the dictionary is a 2D data as $\phi_g \in \mathfrak{R}^{N \times N}$; we order it as vector $\phi_g \in \mathfrak{R}^{N^2}$ in accordance with $y \in \mathfrak{R}^{N^2}$. If we define $\eta = \xi + r$, where the residue η represents errors due to the approximation ξ and the noise r , then (3) can be rewritten as

$$y = D\alpha^{\text{opt}} + \eta. \quad (4)$$

Taking into account the sparsity constraint on the representation coefficient vector, SPDN amounts to solving the following optimization problem:

$$\alpha^{\text{opt}} = \arg \min_{\alpha \in \mathfrak{R}^K} \|\alpha\|_0 \quad \text{subject to} \quad \|y - D\alpha\|_2^2 = \|\eta\|_2^2. \quad (5)$$

In the ideal case, the energy function, which is the difference between the observed noisy image and the noise-free image, is expressed as $\|y - x\|_2^2 = \|r\|_2^2 = N^2 \cdot \sigma_r^2$. In practice, the noise-free image is unknown. Therefore, accounting for the approximation error ξ , the energy function between the observed image and the reconstructed image (which should be as close as possible to the noise-free image) can be expressed as $\|y - D\alpha\|_2^2 = \|\xi + r\|_2^2$. When $0 \leq \|\xi\|_2 \ll \|r\|_2$, we have $\|\eta\|_2^2 = C \cdot N^2 \cdot \sigma_r^2$, where the constant $C \geq 1$ is defined so as to achieve an optimal denoising result. The value of C will be discussed in section 5. Since

we usually do not have the ground truth of the observed image, σ_r should be replaced by its estimation. Therefore, updating this in (5) gives

$$\alpha^{\text{opt}} = \arg \min_{\alpha \in \mathfrak{R}^K} \|\alpha\|_0 \quad \text{subject to} \quad \|y - D\alpha\|_2^2 = C \cdot N^2 \cdot \sigma_r^2. \quad (6)$$

Then, the estimated noise-free image is obtained using

$$\hat{x} = D\alpha^{\text{opt}}. \quad (7)$$

When denoising a large-size image using an overcomplete dictionary $D \in \mathfrak{R}^{N^2 \times K}$, $K > N^2$, with the size of the dictionary increasing in order $O(N^4)$, this considerably raises the computational burden. To cope with this problem, we choose to process the large image using a sliding window (as implemented in Guleryuz (2005a), (2005b)). We overlap patches to reduce blocking artefacts, which contributes to improve the accuracy of the reconstructed image. If the sliding window size is $n \times n$ and its step is s , $y^{N \times N}$ contains $((N - n + 1)/s)^2$ patches of size $n \times n$. For each patch, the coefficient vector α_{ij} is obtained by representing patch y_{ij} with dictionary $D \in \mathfrak{R}^{n^2 \times K}$. In this case, (6) becomes

$$\alpha_{ij}^{\text{opt}} = \arg \min_{\alpha_{ij} \in \mathfrak{R}^K} \|\alpha_{ij}\|_0, \quad \text{subject to} \quad \|\Psi_{ij}y - D\alpha_{ij}\|_2^2 = C \cdot n^2 \cdot \sigma_r^2, \quad (8)$$

where (i, j) designates the locations of patches and Ψ_{ij} is the operator that extracts patches from the image with $y_{ij} = \Psi_{ij}y$.

Accordingly, the denoised image can be obtained as

$$\hat{x} = \left(\sum_{j=1}^{(N-n+1)/s} \sum_{i=1}^{(N-n+1)/s} \Psi'_{ij}x_{ij} \right) \left(\sum_{j=1}^{(N-n+1)/s} \sum_{i=1}^{(N-n+1)/s} \Psi'_{ij}\Psi_{ij} \right)^{-1} \quad \text{with} \quad \hat{x}_{ij} = D\alpha_{ij}^{\text{opt}}, \quad (9)$$

where $\hat{x}_{ij} \in \mathfrak{R}^{n \times n}$ corresponds to the denoised version of each patch, $\hat{x} \in \mathfrak{R}^{N \times N}$ to the final denoised version of the observed image and Ψ'_{ij} to the inverse operation of Ψ_{ij} .

Hence, the image denoising model based on SPDN can be rewritten as

$$\{\alpha^{\text{opt}}, \hat{x}\} = \arg \min_{\{\alpha_{ij} \in \mathfrak{R}^K, x\}} \sum_{ij} \|\alpha_{ij}\|_0 + \lambda \sum_{ij} \|\Psi_{ij}y - D\alpha_{ij}\|_2^2 + \gamma \|y - x\|_2^2, \quad (10)$$

where the parameters λ and γ are penalty factors. The denoising model is expressed as a constrained optimization problem with Lagrange multiplier updating the constraint into penalty terms. It is based on maximum *a posteriori* estimation. This optimization solution means that to find the sparse approximation of the noise-free image through blocking the observed image into patches, every restored patch should obey $\|x_{ij} - y_{ij}\|_2^2 \leq C \cdot n^2 \cdot \hat{\sigma}_r^2$. At the same time, the final reconstructed denoised image satisfies $\|\hat{x} - y\|_2^2 \leq C \cdot N^2 \cdot \hat{\sigma}_r^2$. We can solve this model using the matching pursuit algorithm described in the next subsection.

2.3. Approximation with matching pursuit

The approximation of x_{ij} in the subsection 2.2 can be calculated with the MP algorithm (Mallat and Zhang 1993). The MP algorithm selects the useful atoms in a sequence, depending on the inner product of atom and the image patch. We begin the search with $R^0 y_{ij} = y_{ij}$, after a number of f atoms are selected, there exists residue that we denote by $R^f y_{ij}$. Afterwards, the MP algorithm continues to choose the next atom ϕ_{gf} , which is most correlated with $R^f y_{ij}$ compared to other unused atoms. More precisely, the patch y_{ij} can be decomposed into a sum of atoms with residue $R^p y_{ij}$ as follows:

$$y_{ij} = \sum_{f=0}^{p-1} \langle R^f y_{ij}, \phi_{gf} \rangle \phi_{gf} + R^p y_{ij}. \quad (11)$$

Originally, the residue $\|R^p y_{ij}\|^2$ converges in an exponential rate in finite-dimensional Hilbert spaces. Since the MP algorithm is applied for SPDN here, we set the stop criterion of (11) with our approximation constraint defined above,

$$\|R^p y_{ij}\|^2 = C \cdot n^2 \cdot \hat{\sigma}_r^2. \quad (12)$$

As a consequence, the noise-free patch x_{ij} is approximated as

$$\hat{x}_{ij} = \sum_{f=0}^{p-1} \langle R^f y_{ij}, \phi_{gf} \rangle \phi_{gf}. \quad (13)$$

As can be seen in the above formulations, the main aspect of the SPDN approach consists in recovering the noise-free image by means of setting up the denoising model and atom decomposition. The denoising model, based on the energy function estimation, assures the fidelity of the denoised result. The sliding window method introduced in the model also increases the efficiency of implementation. With an appropriate dictionary, the underlying information in the observed image can be represented with a limited number of atoms and consequently the noise-free image is approximated.

2.4. The design of dictionary

The design of a dictionary reflects prior information about the features of the image. A dictionary can be composed of a single basis or multiple bases depending on the complexity of the contents in the image. The general idea for constructing an appropriate dictionary is to find bases which match comfortably to the smooth regions in the image and can also represent the regions with sharp changes.

In the present study, 2D bases are generated by the Kronecker tensor product of 1D bases. Since it is easier to find an optimal coefficient vector among a large number of possible solutions, the bases are made to be overcomplete. We choose to construct two overcomplete bases: Φ_{2D}^{Haar} and Φ_{2D}^{cos} as

$$\Phi_{2D}^{\text{Haar}} = \Phi_{1D}^{\text{Haar}} \otimes \Phi_{1D}^{\text{Haar}}; \quad \Phi_{2D}^{\text{cos}} = \Phi_{1D}^{\text{cos}} \otimes \Phi_{1D}^{\text{cos}}, \quad (14)$$

where the 1D basis Φ_{1D}^{Haar} and Φ_{1D}^{cos} are designed from pre-defined Haar functions and cosine functions by sampling finely their frequencies and locations.

The atoms of the 1D Haar basis are indexed by a scale variable v and location variable w . We let variables run through the discrete collection of Haar wavelets with dyadic scales $v = 2^j/n$, locations $w = 0, 1, \dots, n - n/2^j$ and $j = 0, 1, \dots, \log_2 n - 1$, where n is the length of the atoms. As an illustration, we define the atom of the 1D Haar basis at scale v and location w by

$$\phi_g^{\text{Haar}}(i) = \varphi(v(i-w)) = \begin{cases} 1, & 0 < v(i-w) \leq 1/2 \\ -1, & 1/2 < v(i-w) \leq 1, \\ 0, & \text{others} \end{cases} \quad i = 1, 2, \dots, n \quad (15)$$

In the basis, denoted as $\Phi_{1D}^{\text{Haar}} = \{\phi_g^{\text{Haar}} \in \mathfrak{R}^n \mid g \in K\}$, the atom ϕ_g^{Haar} only includes one period and is zero padded, so that the atoms constitute a tight frame to decrease approximation errors during linear combination. Likewise, we construct the following 1D cosine basis with a collection of cosinoidal waveforms indexed by a , an angular frequency variable. More precisely

$$\phi_g^{\text{cos}}(i) = \cos(ai), \quad i = 1, 2, \dots, n. \quad (16)$$

Let q be an integer and the set of all cosine atoms is generated with $a = 2\pi g/(qn), g = 0, \dots, qn/2 - 1$, an overcomplete cosine basis, denoted as $\Phi_{1D}^{\text{cos}} = \{\phi_g^{\text{cos}} \in \mathfrak{R}^n \mid g \in K\}$, is

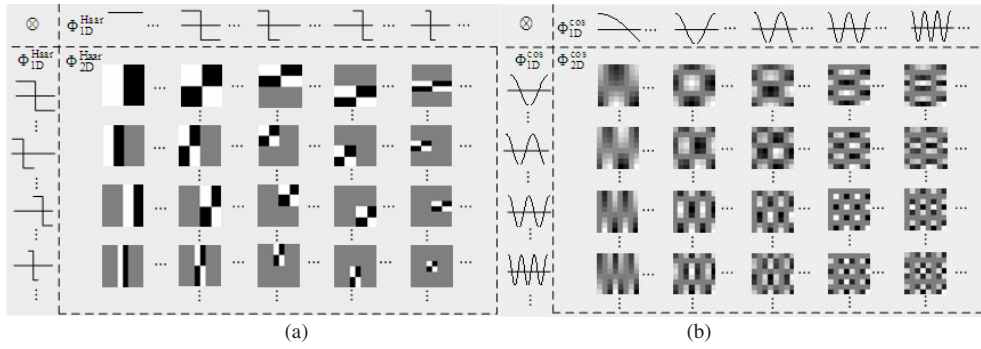


Figure 2. Illustration of the generation of 2D bases. (a) 2D Haar basis constructed from 1D Haar basis, (b) 2D cosine basis constructed from 1D cosine basis.

obtained. This is a q -fold overcomplete basis in which atoms are signals of consecutive cosinoidal waveforms.

Actually, the 2D bases are large arrays formed by taking all possible products between the elements of 1D bases. For instance, with the 1D basis Φ_{1D}^{Haar} of size $n \times \sqrt{K}$, we can obtain Φ_{2D}^{Haar} of size $n^2 \times K$. Figure 2 depicts the generation of 2D bases. As shown in figure 2(a), the atoms of Φ_{1D}^{Haar} are of size $n \times 1$ and they are a set of Haar waveforms with various scales and locations. After implementing the Kronecker tensor product with other atoms, 2D atoms of size $n \times n$ are generated. For an image patch of size $n \times n$, the 2D basis of size $n^2 \times K$ is necessary.

By comparing the Haar basis with the cosine basis in figure 2, it is observed that the intensity distributions of different atoms exhibit different geometrical structures. Atoms of the Haar basis are much sparser; as each atom has no more than three grey levels and its energy is just located in a local region of the atom. In contrast, the structure features of cosine atoms are more complicated, as pixels in each atom include a wide range of grey levels changing gradually in neighbourhood. Because of that, the Haar basis could perform well in reconstructing images with piecewise constant contents or sharp changes while the cosine basis has an advantage of representing images with piecewise smooth contents. The dictionary constructed in the present study consists of both 2D Haar basis and 2D cosine basis.

2.5. Segmentation as a prior

How to project an image on appropriate multiple-bases directly determines approximation accuracy. One basis in the dictionary is generally efficient to represent one content while ineffective for representing the other contents. An image is usually composed of several regions corresponding to different contents, so it is not useful to scan over the whole image with every basis in the dictionary. For that reason, we propose to use segmentation as a guide to locate the edges of regions with a given content and then choose appropriate basis to approximate every contents. To segment an image, we use a detector based on the notion of NSD (Liu *et al* 1995), which detects edges by measuring local NSDs.

As shown in figure 3, for an input signal $S(i)$, a filter $h_1(i)$ operates on it, and then the variation of the $S(i) * h_1(i)$ is calculated:

$$\delta^2(i) = [S(i) * h_1(i)]^2 * h_2(i) - [S(i) * h_1(i) * h_2(i)]^2, \quad (17)$$

where $h_1(i)$ and $h_2(i)$ are linear normalized mean (i.e. rectangular) filters defined by

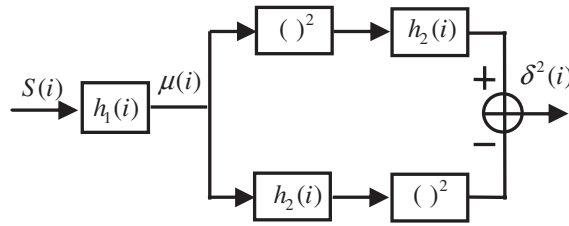


Figure 3. Diagram of the nonstationary degree detector.

$$h_1(i) = h_2(i) = \frac{1}{L} \text{rect} \left(\frac{i}{L} \right), \quad (18)$$

where L is the length of the filters.

When the input signal is stationary at order 2, the output of such a detector is null. Otherwise, the detector outputs higher values, indicating the presence of discontinuities between two stationary segments in the input signal.

For a 2D image, filters of size $L \times L$ are applied to calculate its NSD. Accordingly, the NSD of the input image is given by

$$\delta^2(i) [S(i) * h_1(i)]^2 * h_2(i) - [S(i) * h_1(i) * h_2(i)]^2, \quad (19)$$

where $h_1(i, j)$ and $h_2(i, j)$ are convolutions of two linear normalized mean filters

$$h(i, j) = h(i) * h(j), \quad \text{with } h(i) = \frac{1}{L} \text{rect} \left(\frac{i}{L} \right), \quad h(j) = \frac{1}{L} \text{rect} \left(\frac{j}{L} \right). \quad (20)$$

The output image $\delta^2(i)$ gives prominence to the edges of the input image y , since the edges between different regions represent nonstationary pixels. Therefore, it is easier to extract the edges of image y from image $\delta^2(i)$ by the threshold method. For a volume data, to account for the spatial correlation in the neighbouring slices, the NSD detector can be extended to 3D to achieve more efficient edge detection.

3. Materials and methods

3.1. Acquisition of human cardiac DT-MRI

The DT-MRI acquisitions on *ex vivo* human hearts were performed on the Hospital of Neuro-Cardiology of Lyon. We used a Siemens Avanto 1.5 T MR Scanner with a maximum gradient strength of 40 mT m^{-1} and a slew rate of $200 \text{ T m}^{-1} \text{ s}^{-1}$. The sequence used is a Diffusion Spin Echo EPI, with a Stejskal-Tanner scheme and a b -value of 1000 s mm^{-2} . Ten human hearts were acquired including six healthy ones and four severely diseased ones (ischaemic cardiomyopathy). Each heart was located in a plastic container and fixed by hydrophilic gel to maintain a diastolic shape. This setup has a low dielectric effect and also eliminates unwanted susceptibility artefacts near the boundaries of the heart. In this paper, the LV (left ventricle) long axis, aligning with the axis of the magnet bore, is determined as the intersecting line of the two planes that divide the LV equally into four quadrants from base to apex. The short axis is defined perpendicular to the long axis.

We exercised DT-MRI acquisition protocols defined with different number of diffusion gradient directions ‘N’ and number of excitations ‘NEX’ as follows: (N, NEX) = (6, 1) and (30, 1). We used configurations of cuboctahedron and rhombicuboctahedron for the protocols

with 6 and 30 directions, respectively. Since DT-MRI acquisition for *in vivo* human heart is a great challenge because of cardiac and breathing motions, six gradient directions are more appropriated in clinical application due to short acquisition time. However, high numbers of diffusion gradient directions are more immune to systematic artefacts and noise, with significantly increasing the precision of diffusion tensor and DAIs calculations and reducing rotational variance due to noise propagation (Landman *et al* 2007 Papadakis *et al* 2000). Jones (2004) demonstrated that at least 30 unique sampling orientations are required for a robust estimation of tensor orientation and MD. Therefore, we use *ex vivo* cardiac DT-MRI data acquired with 6 diffusion directions and 30 diffusion directions to evaluate the proposed method.

The diffusion un-weighted image, a reference image, was acquired using the same DTI sequence with the diffusion gradient with b -value = 0 s mm⁻². We perform the zone segmentation of the heart with diffusion un-weighted images for their higher SNR and contrast compared to DWIs. The other acquisition parameters were TE = 86 ms, TR = 8000 ms, slice thickness = 2 mm, slice spacing = 2 mm, slice duration = 130 ms, number of slices = 52. The volume data in each direction was arranged in a 128 × 128 × 52 array where spatial resolution of each voxel is 2 × 2 × 2 mm³.

3.2. Implementation of DT-MRI denoising

The acquired *ex vivo* human cardiac DT-MRI images mainly consist of two regions: the cardiac region of interest and the region outside the heart including black background and hydrophilic gel. The background corresponds to the air outside the organ and the variation represents noise. The intensity of the region with hydrophilic gel should be homogeneous in a noise-free image since the water molecules have the same diffusion character in such a region. Concerning the cardiac region, the information is more complex with anisotropic diffusion in myocardium. Therefore, we choose to apply the Haar basis to the piecewise constant content in the region outside the heart while using the cosine basis for the piecewise smooth content in the heart region. We construct a dictionary composed of a Haar basis of size 64 × 196 and a cosine basis of size 64 × 289. The images in each region, divided into overlapped patches of size 8 × 8, are reconstructed after denoising using the denoising model presented in section 2.2.

Before that, the edges in the diffusion un-weighted image are detected by the NSD algorithm. To take advantage of the spatial correlation in the neighbouring slices, two cubic filters of size 3 × 3 × 3 are applied to the diffusion un-weighted image (figure 4(a)) and its two neighbouring slices. As described in section 2.5, the output of the first stage $y * h_1$ is simply the local mean value of the input image y while the output of the second stage δ^2 is the variance of this mean value. This method detects the edges in the diffusion un-weighted image as shown in figure 4(b). Then, the edge between the two regions can be extracted by boundary tracking in MATLAB. Before that, we convert the image into a binary image based on a global threshold (14595 for figure 4(b)), estimated from the histogram of the image $\delta^2(i, j)$ using two-dimensional entropic thresholding (Abutaleb 1987). Thus, the obtained edge partitions the cardiac DWI into two regions: cardiac region of interest and the region outside the heart (figure 4(c)).

It is well known that the edge detection by thresholding is strongly affected by the criterion for the selection of the threshold value. In the paper, we implement two-dimensional entropic thresholding, which is based on the entropies of the grey level of the pixel and the average grey level of its neighbourhood. Since the NSD detector has enhanced the edges, the image $\delta^2(i, j)$ presents high edge contrast. Therefore, it is feasible to detect the edge

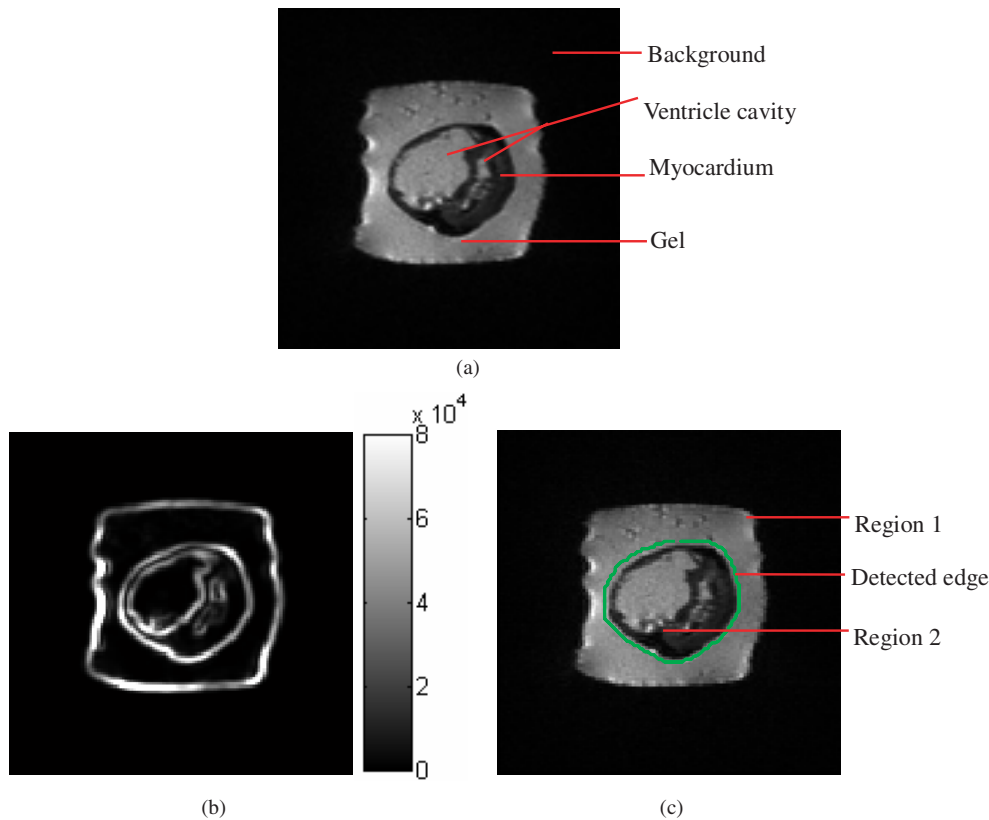


Figure 4. Edge detection of cardiac DWI using the nonstationary degree detector. (a) The input image of the NSD: diffusion un-weighted image, (b) the output image of the NSD, (c) the DWI is segmented into two regions with the edge obtained from (b).

between the two regions using a global threshold. In experiments, two-dimensional entropic thresholding performs well on selecting a proper threshold and detects the edge without breaks or undesirable edge fragments. However, the double thresholding method, local thresholding and also multi-stage thresholding may give more adaptive and robust results but they will increase computation complexity and be more time consuming. Anyway, segmentation is an open question and there are quite a number of segmentation methods. Among them, edge detection by thresholding as we used is just a simple one and this is not our major topic.

It has been demonstrated that the noise in DWI presents a Rician distribution in which random variable square is a non-central chi-square distribution. The means of two independent Gaussian noises come from the real and imaginary channels of DT-MRI. Typical DWI contains a non-signal region in the background corresponding to the air outside the organ. In such a region, it is assumed that $x^2 = 0$ and the variances are all caused by noise. The Rician noise level σ_r used in (6) can be estimated by the square root of half expectation of the squared intensity values in the non-signal regions of the corrupted image as $\hat{\sigma}_r = \sqrt{\frac{1}{2}E(y^2)}$ (Nowak 1999). For all the experiments in the cardiac DWIs, the same parameter setting has been used for factor $C = 1.13$, patch size 8×8 and filters size $3 \times 3 \times 3$.

The effectiveness of the proposed method in denoising cardiac DT-MRI is compared with two conventional methods: PDE-based nonlinear diffusion denoising (Catté *et al* 1992) and a wavelet-based prior model from Pizurica *et al* (2003). The parameters of all the methods

have been experimentally optimized to produce the best denoising results with high SNR and contrast in profile. For PDE-based denoising, its parameters includes diffusion function $g(\nabla I) = \exp((\|\nabla I\|/k)^{-2})$, variance of Gaussian to convolve gradient and iteration number, while the parameters for the wavelet-based denoising are the threshold multiplication factor and window size (parameter definitions can be found in the above references).

3.3. Denoising performance evaluation

We generate a simulated heart-like-shaped image as shown in figure 5(a) to evaluate the behaviour of the SPDN algorithm with the dictionary of multiple bases and the NSD detector. The simulated heart-like-shaped image presents two structures: the central part of the image exhibits a heart shape akin to left and right ventricles while the rest of the image represents the gel and air regions in cardiac DWI. The intensity of the left ventricular region is made to change gradually from inside to outside to simulate the diffusion difference of the fibres from the endocardium to the epicardium. We corrupt the simulated image with Rician noise of different levels $\sigma_r \in \{5, 10, 15, 20, 25, 30\}$ with respect that the intensity of the noise-free image ranges from 0 to 221. As the noise-free image is known in advance for a simulated image, the SNR is defined as (Pizurica *et al* 2003, Awate and Whitaker 2007) $10 \cdot \log_{10}(\text{Var}(x)/\text{Var}(\tilde{x} - x))$, where $\text{Var}(\cdot)$ denotes the variance of the intensities of the image, x the noise-free image and \tilde{x} either the noisy image y or the denoised image \hat{x} as defined in section 2.2.

To assess the performance of the proposed denoising method on cardiac DWIs, the SNR calculated on DWIs is the most intuitive measurement. Since we do not know the ground truth of cardiac DWIs, the SNRs of the cardiac DWIs are computed over two regions of interest (ROI). The conventional MR image SNR criterion is $\text{SNR} = 10 \cdot \log_{10}(\tilde{x}_{\text{mean}}^2/\sigma_r^2)$ (Nowak 1999), where \tilde{x}_{mean} designates the mean of the intensity in the ROI of the myocardium, and σ_r denotes the standard deviation of the noise calculated from the air region in the image. In addition, we also propose to apply another definition $\text{SNR}_2 = 10 \cdot \log_{10}(\sigma_M^2/\sigma_G^2)$ in order to account for the very granular aspect of our DWIs and blurring effects in different regions eventually produced by denoising algorithms. In this definition, we measure a signal variance to noise variance ratio, where σ_M^2 denotes the variance of the signal in the ROI of myocardium and σ_G^2 denotes the variance of the noise in the ROI of the gel region. Because the intensity of the gel region in DWI is homogeneous in principle as discussed in section 3.2, this leads us to calculate the noise from the intensity variance of the gel in this definition.

To further get insights into the denoising performance of the proposed method, a set of slices are selected around the equatorial slice of each heart to measure the DT-MRI indices before and after denoising. In the paper, the FA map, MD map, directionality map and fibre architecture are employed to qualitatively illustrate the different performance of the three denoising methods. Furthermore, we apply the quantitative statistics on the negative eigenvalue count, mean and variance (Var) of FA, MD, CI and fibre length to give a comprehensive analysis. These maps and their corresponding statistical analyses are implemented with software Bioimagesuite (Papademetris *et al* <http://www.bioimagesuite.org>).

In the presence of noise and artefacts, the tensors at some voxels may yield negative eigenvalues that are not physically possible and we should exclude these voxels from the diffusion maps and statistics. Denoising allows decreasing the number of voxels with negative eigenvalues. FA and MD are two parameters derived from the non-negative eigenvalues of diffusion tensors, which describe the anisotropy and the diffusivity of diffusion, respectively. FA measures the variability of water mobility in different directions and is defined as $\text{FA} = \left\{ \frac{3[(\lambda_1 - \bar{\lambda})^2 + (\lambda_2 - \bar{\lambda})^2 + (\lambda_3 - \bar{\lambda})^2]}{2(\lambda_1^2 + \lambda_2^2 + \lambda_3^2)} \right\}^{1/2}$, where $\bar{\lambda}$ is quantified as the mean of the three eigenvalues

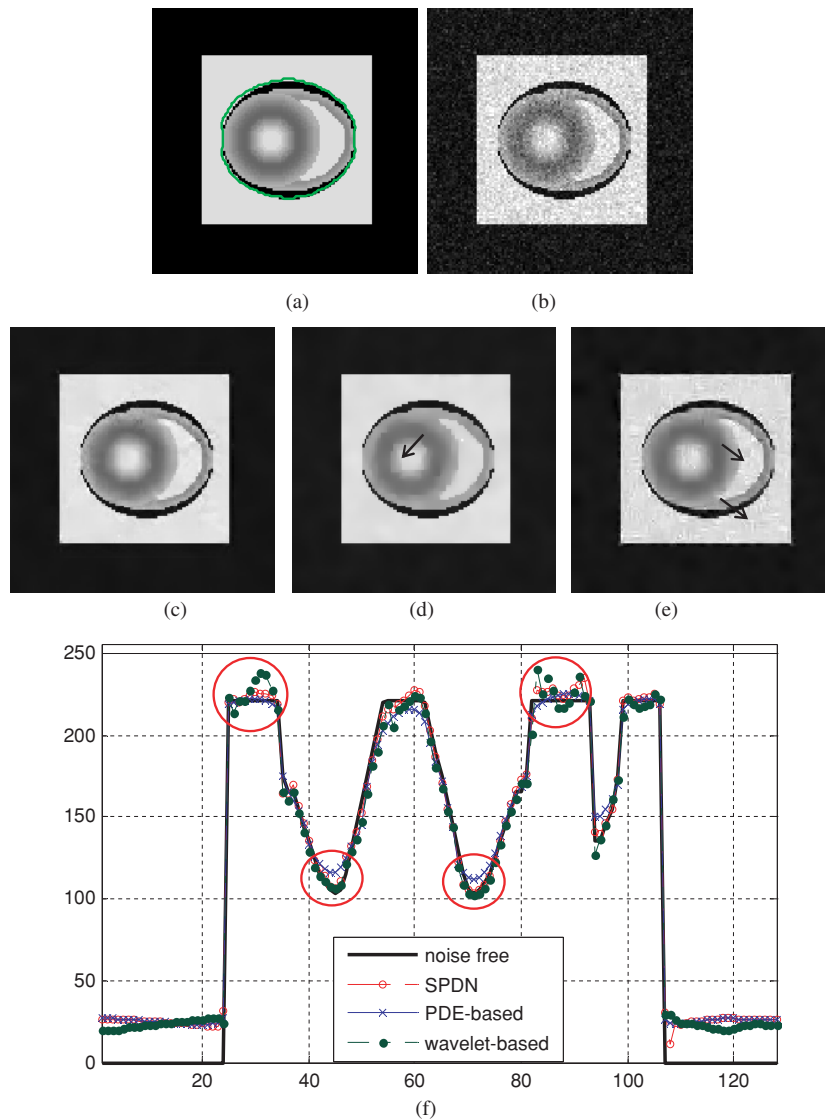


Figure 5. Denoising results on the simulated image with the Rician noise level $\sigma_r = 20$. (a) Noise-free image. (b) Noisy image, SNR = 13.8 dB. Images denoised using (c) SPDN, SNR = 17.9 dB, (d) PDE-based nonlinear diffusion denoising, SNR = 17.7 dB and (e) wavelet-based denoising, SNR = 16.7 dB. The line profiles corresponding to images (a) and (c)–(e) are shown in (f). Pixels around the arrow heads in images (d) and (e) exhibit obvious fine structure losses and artefacts, and pixels in the circles in (f) are differences to be noted in denoising results.

of the diffusion tensor $\lambda_1, \lambda_2, \lambda_3$. It ranges from 0 for isotropic diffusion to 1 for completely anisotropic diffusion. MD, denoted as $\bar{\lambda}$, indicates the mean diffusivity of water molecules, which reflects the redistribution of intracellular and extracellular space volumes.

Directionality map, CI and fibre reconstruction all reflect the orientation distribution of diffusion tensors defined by the principal eigenvectors. Directionality map, also called the colour tensor, represents the principal eigenvector by means of a colour representation: the x

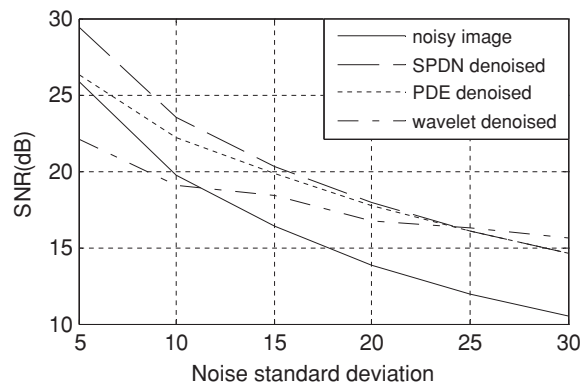


Figure 6. Comparison of denoising results obtained with the three methods in terms of SNR in the case of the simulated image with different noise levels σ_r ranging from 5 to 30.

(left–right) component as red, the y (anterior–posterior) component as green and the z (apex–base) component as blue, and the brightness is modulated by FA in the paper. CI estimates the orientation coherence of fibres and is defined as the mean dot product $CI = \frac{1}{26} \sum_{ij} v \cdot v_{ij}$ of the eigenvectors v and its 26 neighbouring voxels v_{ij} . A high CI value reflects directional coherence of fibres in neighbouring voxels. It is well known that the heart fibre represents a helix structure with the transmural gradient of fibre inclination angles. Fibre regularity, fibre count and also fibre lengths and angles are important information in DT-MRI applications.

4. Results

4.1. Application to simulated images

Figures 5(a) and (b) show the simulated noise-free and noisy ($\sigma_r = 20$) images. In figure 5(a), the contour in green represents the edge obtained with the NSD detector. The results of denoising using the different methods are illustrated in figures 5(c)–(e) and their profiles' comparison are shown in figure 5(f). The SNR of the denoised image in figure 5(c) is improved by 4.1 dB compared to the corrupted image, while the PDE-based denoising increases the SNR by 3.9 dB and the wavelet-based filter increases the SNR by 2.9 dB as represented in figures 5(d) and (e).

The proposed SPDN method (figure 5(c)) almost suppresses the noise while keeping a very good spatial resolution (sharper edges are preserved) and high contrast (the denoised image almost has the same dynamic range as the original image). In contrast, PDE-based denoising leads to more fine structure losses (see the region indicated by the arrow in figure 5(d)) and its contrast preservation is also worse than SPDN as can be observed in the peaks and valleys of the profile shown in figure 5(f). On the other hand, wavelet-based denoising introduces obvious artefacts, especially in the high intensity region as indicated by the two arrows in figure 5(e). SPDN leads to less contrast loss and fewer artefacts than the other two methods. This is particularly clear when comparing their profiles in figure 5(f). More quantitatively, figure 6 gives the comparison between the three methods in terms of SNR for different noise levels. It is seen that the proposed method and PDE-based method always yield better results than the wavelet-based method except for the noise level $\sigma_r = 30$, to which the obtained SNRs are close.

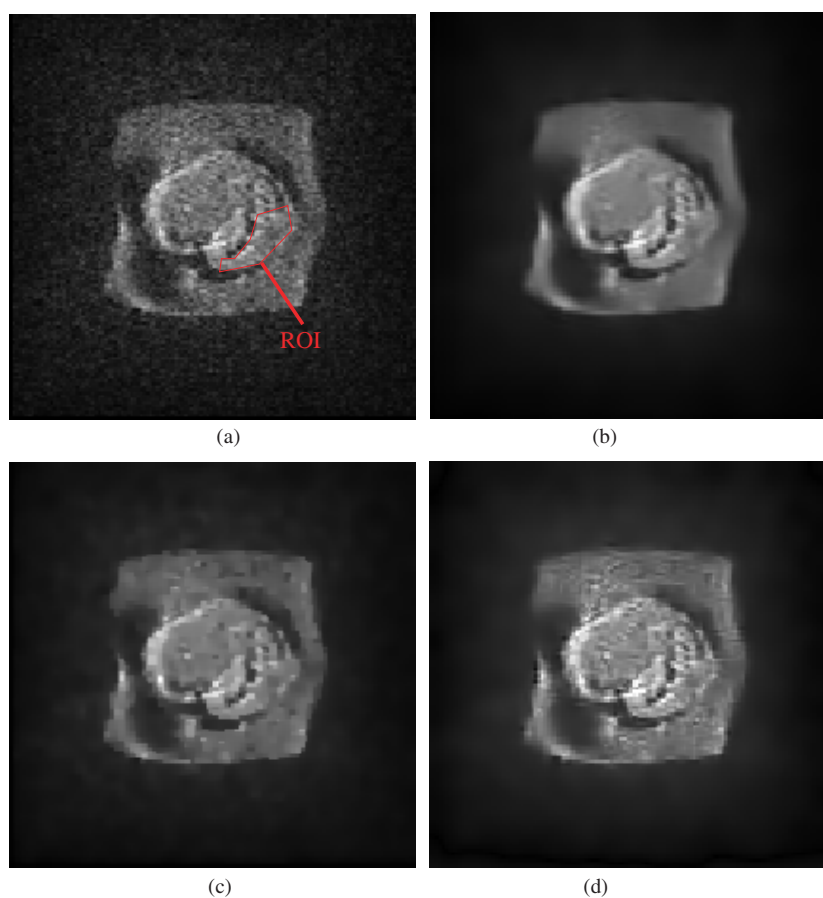


Figure 7. Denoising results on a DWI of *ex vivo* human cardiac DT-MRI datasets with $(N, NEX) = (6, 1)$ (a) Noisy DWI with $SNR = 18.2$ dB, $SNR_2 = 4.5$ dB. Image denoised using (b) SPDN, $SNR = 25.4$ dB, $SNR_2 = 10.4$ dB; (c) PDE-based smoothing, $SNR = 24.3$ dB, $SNR_2 = 8.2$ dB; and (d) wavelet-based filter, $SNR = 23.2$ dB, $SNR_2 = 6.6$ dB. The line profiles in (e)–(h) correspond to the images in (a)–(d).

4.2. Application to human cardiac DT-MRI

The results of denoising the real DWIs using the proposed method and PDE- and wavelet-based denoising techniques are demonstrated in figure 7. Figure 7(a) represents a DWI of *ex vivo* diseased human cardiac DT-MRI data with $(N, NEX) = (6, 1)$. The proposed method (figure 7(b)) produces the best performance with the highest SNRs ($SNR = 25.4$ dB, $SNR_2 = 10.4$ dB) as the ROI marked in figure 7(a). This ROI corresponds to the myocardial region of the left ventricle. In contrast, the PDE-based method presents some ‘washing effect’ by drastically modifying the grey level aspect of the original image and details and its SNRs of the result are $SNR = 24.3$ dB, $SNR_2 = 8.2$ dB. Concerning the wavelet-based method, it gives results visually similar to those of the proposed method, but with smaller SNRs ($SNR = 23.2$ dB, $SNR_2 = 6.6$ dB). The performance difference between the three methods can be further assessed with the profiles in figures 7(e)–(h). Using a PC with Intel Pentium

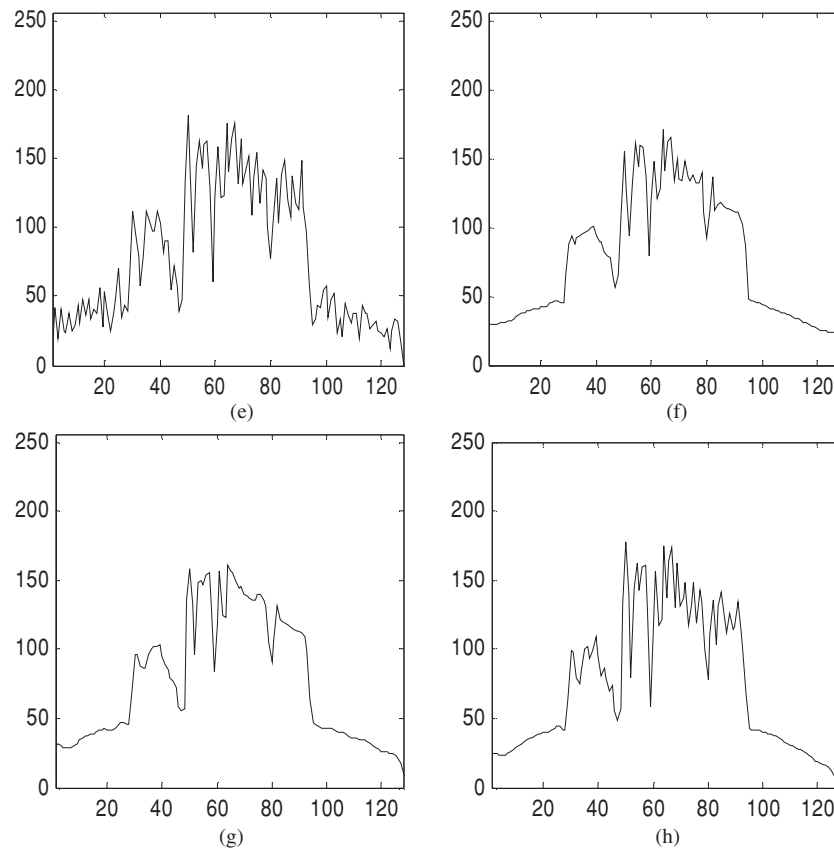


Figure 7. (Continued.)

Dual E2140 1.60 GHz, 2.00 GB memory, windows XP platform, it takes about 4 min and 20 s for denoising a 3D DT-MRI dataset of size $128 \times 128 \times 52$ using the proposed method.

Figures 8 and 9 show the FA maps, MD maps and directionality maps of a slice of the heart in figure 7 with $(N, NEX) = (6, 1)$ and $(30, 1)$, respectively, calculated before and after denoising with the three methods. Their quantitative analyses are given in table 1. In figure 8(a), the FA map before denoising exhibits noticeable noise-induced granular aspects and even black stains because of negative eigenvalue, which are also present in the MD maps (figure 8(b)) and directionality maps (figure 8(c)). With PDE-based and wavelet-based denoising, many graininess artefacts remain with high FA and the negative eigenvalues are almost not removed. In contrast, SPDN removes most of the negative eigenvalues and artefacts in the maps. The directionality maps indicate that the principle eigenvectors are more regularly oriented as the colour of neighbouring voxels changes gradually with less discontinuity after denoising the DWIs using the proposed method. Note that the maps with $(N, NEX) = (30, 1)$ exhibit the same problems, but that granular aspects and negative eigenvalues are less severe than in the maps derived from $(6, 1)$, as can be observed in figure 9. It is found that SPDN denoising yields the visually best maps than the other two methods, by removing more negative eigenvalues and regularizing the direction distribution of diffusion tensors.

The above visual analyses are confirmed by the quantitative results in table 1. We observe that denoising decreases the number of negative eigenvalues (the number of voxels with positive eigenvalue is denoted by 'Available voxels' in the tables) and the FA mean and its

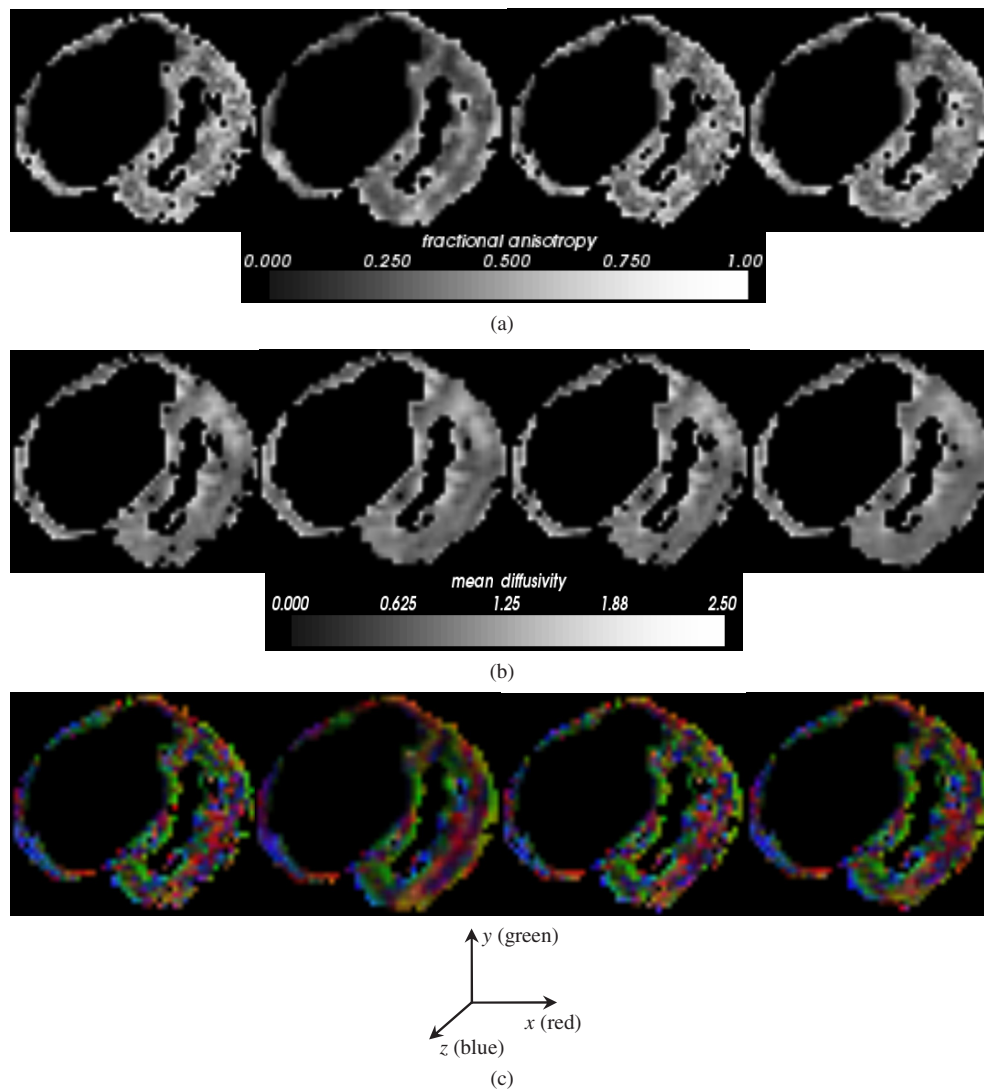


Figure 8. DT-MRI index maps of a diseased heart of scheme (6, 1). (a) FA maps, (b) MD ($10^{-3} \text{ mm}^2 \text{ s}^{-1}$) maps and (c) directionality maps. From left to right, the maps correspond to noisy DT-MRI, and denoised DT-MRIs obtained with SPDN, PDE-based and wavelet-based denoising, respectively.

variance while increasing the CI mean. Moreover, the indices of scheme (6, 1) after denoising approximate to the values of (30, 1). For instance, after denoising the data of scheme (6, 1) with SPDN, its FA mean decreases from 0.443 to 0.350, compared with the value of 0.429 and 0.414 for the other methods, 0.350 being the closest to the FA mean (0.300) of (30, 1). Generally, among the three methods, the SPDN produces the most significant improvements on indices: -21% for FA mean, -3% for MD mean and 52% for CI mean for data of scheme (6, 1). The denoising effect on the data of scheme (30, 1) are -13% for FA mean, -1% for MD mean and 28% for CI mean. Meanwhile, the decrease of MD is tiny compared with the other indices.

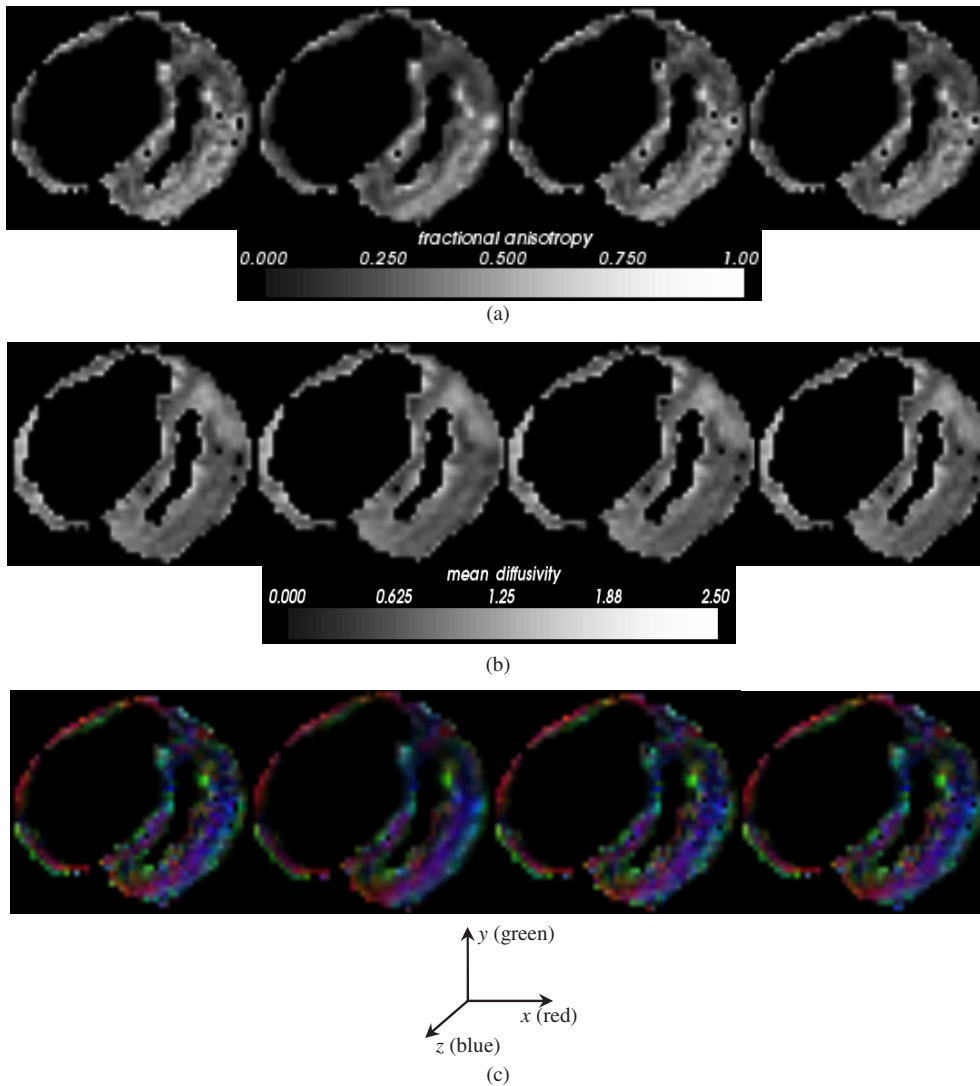


Figure 9. DT-MRI index maps of the same diseased heart in figure 8, but of scheme (30, 1). (a) FA maps, (b) MD ($10^{-3} \text{ mm}^2 \text{ s}^{-1}$) maps and (c) directionality maps. From left to right, the maps correspond to noisy DT-MRI, and denoised DT-MRIs obtained with SPDN, PDE-based and wavelet-based denoising, respectively.

Figure 10 renders the fibres (in directionality colour map) of the heart with ten slices around the slice in figure 7. Table 2 gives the indices of the fibres. The following thresholds are used in fibre tracking: FA 0.05 (this FA threshold was chosen empirically in order to track more fibres), minimum fibre length 5 mm and maximum fibre angle 60° . We observe that without denoising, the tracked fibres are in disorder and intermittent, while after denoising, fibre tracking can smoothly construct the curvature of the trajectories, especially for the data of scheme (6, 1) in figure 10(a). Compared with original 2851 fibres before denoising (figure 10(a) left), a number of 3123 fibres are tracked from cardiac DT-MRI denoised with

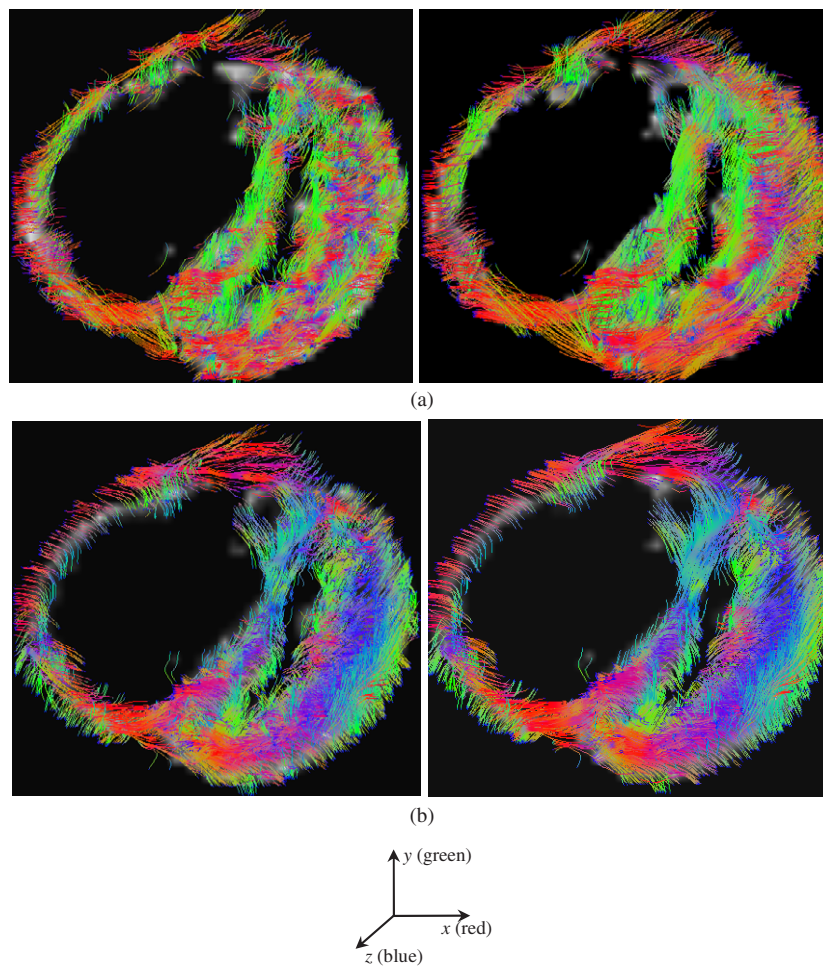


Figure 10. Myocardium fibre tracking before and after denoising the heart shown in figures 8 and 9, with (a) the DT-MRI of scheme (6, 1) and (b) of scheme (30, 1). Left column: with noisy DT-MRIs. Right column: with DT-MRIs denoised using SPDN.

SPDN (figure 10(a) right) and the mean of fibre length increases from 6.6 mm to 7.6 mm. The fibres also run more regularly with the mean of fibre angle decreased from 16.2° to 12.2° and are more consistent with fibre organization reconstructed from the data of scheme (30, 1) (figure 10(b)). As for DT-MRI data of scheme (30, 1), denoising with the proposed method makes the fibre architecture more delicate and precise, providing more structure details with more tracked fibres as listed in table 2.

Finally, denoising results on the other nine hearts of scheme (30, 1) (three slices of each heart) with the proposed method are reported in table 3. The results are consistent with those in table 1: the decrease of FA mean and MD mean range from -3% to -21% and 0 to -4% while the increase of CI mean ranges from 5 to 39%. It is interesting to note that, in table 3, the MD means of the diseased heart are higher than the normal hearts.

Table 1. Comparison of the denosing methods in terms of available voxels, fractional anisotropy, mean diffusivity and fibre coherent index, for the images shown in figures 8 and 9.

Samples	Voxels in mask	Available voxels	FA		MD ($10^{-3} \text{ mm}^2 \text{ s}^{-1}$)		CI		
			Mean	Var	Mean	Var	Mean	Var	
(6, 1)	Noisy	668	613	0.443	0.027	0.983	0.094	0.653	0.091
	SPDN		656	0.350	0.023	0.957	0.092	0.992	0.123
	PDE-based		621	0.429	0.027	0.976	0.097	0.701	0.097
	Wavelet-based		656	0.414	0.026	0.974	0.082	0.743	0.106
(30, 1)	Noisy	677	670	0.300	0.021	0.827	0.089	0.938	0.129
	SPDN		674	0.261	0.018	0.818	0.090	1.198	0.118
	PDE-based		670	0.292	0.020	0.826	0.090	0.944	0.133
	Wavelet-based		670	0.283	0.020	0.826	0.089	1.003	0.131

Table 2. Quantitative analysis of the fibre architectures shown in figure 10. For each scheme, the first line corresponds to the DT-MRI data before denosing and the second line to the data after denosing using SPDN.

Samples	Fibre count	Volume (mm^3)	FA		MD ($10^{-3} \text{ mm}^2 \text{ s}^{-1}$)		Fibre length (mm)		Fibre angle ($^\circ$)	
			Mean	Var	Mean	Var	Mean	Var	Mean	Var
(6, 1)	2851	8551	0.360	0.010	0.769	0.028	6.615	30.734	16.210	16.421
	3123	8987	0.296	0.009	0.750	0.026	7.593	31.222	12.262	16.171
(30, 1)	3069	8885	0.271	0.008	0.635	0.024	6.236	22.305	10.416	16.685
	3155	8956	0.245	0.007	0.627	0.024	6.202	19.875	8.170	13.755

5. Discussion and conclusion

As observed in the preceding section, after denosing the DT-MRI, the FA mean and its variance decrease and the CI mean increases obviously. It also alters fibre tracking by increasing the number of tracked fibres and fibre lengths. These are in agreement with the observations reported in previous studies (Basser and Pajevic 2000, Koay *et al* 2007) that the presence of noise induce negative eigenvalues, positive error in FA, disorder of the eigenvectors and tracked fibres. These errors in DT-MRI indices are all because of the bias in the principal eigenvalues and principal eigenvectors calculated from the noisy DT-MRI.

However, as two diffusion indices are computed from eigenvalues, it is observed that MD means vary a little before and after denosing while FA means change a lot. This is due to the definition of the two indices. So FA is intrinsically more susceptible to noise contamination than MD, as reflected by its larger bias and error variance for the same SNR levels (Basser and Pierpaoli 1998). We can also find that the denosing effects on the indices of scheme (6, 1) are more obvious than those of (30, 1) and denosing makes the indices of scheme (6, 1) approximate to those of (30, 1). This is because a high number of diffusion gradient directions and longer acquisition time are more immune to systematic artefacts and noise. Therefore, DT-MRI indices generated from data of scheme (30, 1) provide references for evaluating the denosing performance on data of scheme (6, 1).

As indicated in table 3, the MD means for a diseased heart are higher than the normal hearts. This finding is consistent with the findings of the DT-MRI study of Wu and Tseng (2006). They report that FA will decrease if the organization of tissue structure is destroyed and

Table 3. Results of denoising using SPDN on the other nine hearts of scheme (30, 1). For each heart, the first line corresponds to the DT-MRI data before denoising and the second line to the data after denoising using SPDN.

Heart	Voxel in mask	Available voxel	FA		MD (10^{-3} mm ² s ⁻¹)		CI	
			Mean	Var	Mean	Var	Mean	Var
Normal 1	3057	2923	0.326	0.024	0.654	0.113	1.000	0.101
		3057	0.303	0.025	0.624	0.118	1.195	0.115
Normal 2	2375	2314	0.338	0.023	0.633	0.174	0.951	0.147
		2344	0.293	0.019	0.624	0.172	1.233	0.141
Normal 3	2373	2370	0.223	0.008	0.596	0.041	1.123	0.146
		2372	0.216	0.007	0.598	0.040	1.173	0.146
Normal 4	2827	2820	0.302	0.013	0.587	0.089	0.823	0.211
		2826	0.252	0.007	0.578	0.085	1.141	0.316
Normal 5	2056	2039	0.270	0.015	0.699	0.058	1.010	0.126
		2046	0.244	0.012	0.696	0.055	1.197	0.125
Normal 6	3086	3059	0.253	0.017	0.800	0.118	0.831	0.159
		3075	0.209	0.013	0.789	0.118	1.137	0.202
Diseased 1	2683	2668	0.312	0.018	0.836	0.073	0.987	0.123
		2679	0.259	0.016	0.832	0.067	1.118	0.124
Diseased 2	2666	2659	0.270	0.012	0.760	0.038	1.097	0.111
		2664	0.213	0.008	0.770	0.037	1.418	0.068
Diseased 3	2059	2002	0.303	0.022	0.821	0.090	0.919	0.109
		2020	0.263	0.018	0.811	0.091	1.148	0.106

MD is significantly increased in the infarct (ischaemia) zone in the human heart. Endocardial area is most susceptible to ischaemia. Therefore, positive angles had the most severe loss in the infarct zone. Since the exact ischaemia zones are unknown for us now, more researches are necessary for demonstrating that.

We compare the proposed method with two common filters for denoising DT-MRI. According to the results, our proposed method consistently outperforms the PDE- and wavelet-based filters in both qualitative and quantitative analyses. The method we have proposed for denoising human cardiac DT-MRI is based on combining sparse representation with a segmentation scheme using the NSD detector. The sparse representation exploits the unique property of atom decomposition to reconstruct the underlying noise-free image. The use of the NSD detector allows the different contents of the image to be segmented, which makes the generation of the dictionary more adaptive and also improves the denoising result. The obtained results show that the proposed method effectively reduces the noise in human cardiac DT-MRI while preserving image details and contrast and improving the calculation accuracy of diffusion tensors as well as the principal eigenvector field of the heart. That would allow a more precise and robust fibre tracking of the myocardium. In the future work, the proposed denoising method can be further optimized by designing more specific dictionaries with respect to the particular features of human cardiac DWIs, or by extending the SPDN method to 3D data.

In the proposed denoising method, there are three adjustable parameters: factor C in (8), patch size and filter window size L . The parameter C influences the denoising results, but rather slightly. C should be greater than 1. However, when C is too great, over-filtering can occur. In practice, the values of C between 1.05 and 1.15 yield similar denoising results, as the SNR difference between the denoised results obtained with $C = 1.15$ and 1.05 is less

than 0.05 dB for the simulated images while the differences of SNR and SNR₂ are less than 0.3 dB and 0.2 dB separately for real cardiac images. In our experiments, setting $C = 1.13$ achieves the near optimal results for real cardiac images with a tradeoff between SNR and SNR₂. Concerning the patch size, it is, in the field of image processing, well known that spatial correlation in an image does not exceed 16×16 . Therefore, one often simply chooses a patch size among 8×8 , 16×16 and 32×32 . In our present study, 8×8 is a good choice in terms of denoising effects (SNR and contrast in profile) and computation time (a larger patch size will be more time-consuming with rather close results). As for the filter window size L , it is generally chosen as 3, 5 or 7 according to the image in question. Here we use filters of size $3 \times 3 \times 3$ for cardiac DT-MRI and 3×3 for a simulated image since they produced the best edge enhancement for the images studied.

The objective of the proposed segmentation is to obtain the myocardium region. The proposed segmentation process is based on using the notion of NSD, which is particularly powerful for detecting the presence of discontinuities between two regions in the input image. For the *ex vivo* cardiac DT-MRI data investigated in the present study, the proposed segmentation always works well on the diffusion un-weighted image. In principle, it could still work in case greater contrast variations are present throughout the image. This aspect should be further investigated for *in vivo* human cardiac DT-MRI. However, no matter for *in vivo* and *ex vivo* cardiac image, it is better to apply segmentation as a guide to the choice of the basis when denoising cardiac DT-MRI using the SPDN method. It also supplies an idea for using SPDN to general image processing.

Acknowledgments

This work is supported by the National Natural Science Foundation of China (60777004) and International S&T Cooperation Project of China (2007DFB30320). The authors thank Stanislas Rapacchi for his help in acquiring the data, and many other researchers in CREATIS-LRMN for their helpful discussions and comments in this investigation.

References

- Abutaleb A S 1987 Automatic thresholding of gray-level pictures using two dimensional entropy *Comput. Vis. Graph. Image Process.* **47** 22–32
- Aharon M, Elad M and Bruckstein A 2006 K-SVD: an algorithm for designing overcomplete dictionaries for sparse representation *IEEE Trans. Signal Process.* **54** 4311–22
- Alexander M E, Baumgartner R, Summers A R, Windischberger C, Klarhoefer M, Moser E and Somorjai R L 2000 A wavelet-based method for improving signal-to-noise ratio and contrast in MR images *Magn. Reson. Imaging* **18** 169–80
- Arsigny V, Fillard P, Pennec X and Ayache N 2006 Log-Euclidean metrics for fast and simple calculus on diffusion tensors *Magn. Reson. Med.* **56** 411–21
- Awate S P and Whitaker R T 2007 Feature-preserving MRI denoising: a nonparametric empirical Bayes approach *IEEE Trans. Med. Imaging* **26** 1242–55
- Basser P J, Mattiello J and LeBihan D 1994 MR diffusion tensor spectroscopy and imaging *Biophys. J.* **66** 259–67
- Basser P J and Pajevic S 2000 Statistical artifacts in diffusion tensor MRI (DTMRI) caused by background noise *Magn. Reson. Med.* **44** 41–50
- Basser P J and Pierpaoli C 1998 A simplified method to measure the diffusion tensor from seven MR images *Magn. Reson. Med.* **39** 928–34
- Basu S, Fletcher T and Whitaker R 2006 Rician noise removal in diffusion tensor MRI *MICCAI LNCS* **4190** 117–25
- Catte F, Lions P L, Morel J M and Coll T 1992 Image selective smoothing and edge detection by nonlinear diffusion *SIAM J. Numer. Anal.* **29** 182–93
- Chen B and Edward W 2005 Noise removal in magnetic resonance diffusion tensor imaging *Magn. Reson. Med.* **54** 393–407

- Chen S S, Donoho D L and Saunders M A 1998 Atomic decomposition by basis pursuit *SIAM J Sci. Comput.* **20** 33–61
- Elad M and Aharon M 2006 Denoising via sparse and redundant representations over learned dictionaries *IEEE Trans. Image Process.* **15** 3736–45
- Galban C J, Maderwald S, Uffmann K and Ladd M E 2005 A diffusion tensor imaging analysis of gender differences in water diffusivity within human skeletal muscle *NMR Biomed.* **18** 489–98
- Gerig G and Kubler O 1992 Nonlinear anisotropic filtering MRI data *IEEE Trans. Med. Imaging* **11** 221–33
- Gilboa G, Sochen N and Zeevi Y Y 2004 Image enhancement and denoising by complex diffusion processes *IEEE Trans. Pattern Anal. Mach. Intell.* **26** 1020–36
- Gorodnitsky I F and Rao B D 1997 Sparse signal reconstruction from limited data using FOCUSS: a re-weighted minimum norm algorithm *IEEE Trans. Signal Process.* **45** 600–16
- Granai L and Vandergheynst P 2004 Sparse decomposition over multi-component redundant dictionaries *IEEE Proc of Multimedia Signal Processing, Workshop on MMSP*
- Gudbjartsson H and Patz S 1995 The Rician distribution of noisy MRI data *Magn. Reson. Med.* **34** 910–4
- Guleryuz O G 2005a Nonlinear approximation based image recovery using adaptive sparse reconstructions and iterated denoising: part I. Theory *IEEE Trans. Image Process.* **15** 539–53
- Guleryuz O G 2005b Nonlinear approximation based image recovery using adaptive sparse reconstructions and iterated denoising: part II. Adaptive algorithms *IEEE Trans. Image Process.* **15** 554–71
- Hamameh G and Hradsky J 2007 Bilateral filtering of diffusion tensor magnetic resonance images *IEEE Trans. Image Process.* **16** 2463–75
- Jones D K 2004 The effect of gradient sampling schemes on measures derived from diffusion tensor MRI: a Monte Carlo study *Magn. Reson. Med.* **51** 807–15
- Koay C G, Chang L C, Pierpaoli C and Basser J P 2007 Error propagation framework for diffusion tensor imaging via diffusion tensor representations *IEEE Trans. Med. Imaging* **26** 1017–34
- Landman B A, Farrell J D, Jones C K, Smith S A, Prince J L and Moria S 2007 Effects of diffusion weighting schemes on the reproducibility of DTI-derived fractional anisotropy, mean diffusivity, and principal eigenvector measurements at 1.5 T *NeuroImage* **36** 1123–38
- Liu W Y, Magnin I E and Gimenez G 1995 Un nouvel opérateur pour la détection de rupture dans des signaux bruités *Trait. Signal* **12** 226–36
- Macovski A 1996 Noise in MRI *Magn. Reson. Med.* **36** 494–7
- Mallat S and Zhang Z 1993 Matching pursuits with time-frequency dictionaries *IEEE Trans. Signal Process.* **41** 3397–415
- Nowak R D 1999 Wavelet based Rician noise removal for magnetic resonance imaging *IEEE Trans. Image Process.* **8** 1408–19
- Papadakis N G, Murrills C D, Hall L D, Huang C L and Carpenter T A 2000 Minimal gradient encoding for robust estimation of diffusion anisotropy *Magn. Reson. Imaging* **18** 671–9
- Papademetris X, Jackowski M, Rajeevan N, Constable R T and Staib L H BioImage Suite: an integrated medical image analysis suite Section of Bioimaging Sciences, Department of Diagnostic Radiology, Yale School of Medicine <http://www.bioimagesuite.org>
- Perona P and Malik J 1990 Scale-space and edge-detection *IEEE Trans. Pattern. Anal. Mach. Intell.* **12** 629–39
- Pham T V and Smeulders A W M 2006 Sparse representation for coarse and fine object recognition *IEEE Trans. Pattern. Anal. Mach. Intell.* **28** 555–67
- Pizurica A, Philips W, Lemahieu I and Acheroy M 2003 A versatile wavelet domain noise filtration technique for medical imaging *IEEE Trans. Med. Imaging* **22** 323–31
- Schwartz E D, Duda J, Shumsky J S, Cooper E T and Gee J 2005 Spinal cord diffusion tensor imaging and fiber tracking can identify white matter tract disruption and glial scar orientation following lateral funiculotomy *J. Neurotrauma* **22** 1388–98
- Scollan D F and Holmes A 2000 Reconstruction of cardiac centricular geometry and fiber orientation using magnetic resonance imaging *Ann. Biomed. Eng.* **28** 934–44
- Starck J L, Elad M and Donoho D L 2005 Image decomposition via the combination of sparse representations and a variational approach *IEEE Trans. Image Process.* **14** 1570–82
- Wirestam R and Bibic A 2006 A denoising of complex MRI data by wavelet-domain filtering: application to high-B-value diffusion-weighted imaging *Magn. Reson. Med.* **56** 1114–20
- Wu M T and Tseng W Y 2006 Diffusion tensor magnetic resonance imaging mapping the fibre architecture remodelling in human myocardium after infarction *Circulation* **114** 1036–45